Detection of Exocometary CO within the 440 Myr Old Fomalhaut Belt: A Similar CO+CO$_2$ Ice Abundance in Exocomets and Solar System Comets

L. Matrà[1], M. A. MacGregor[2], P. Kalas[3,4], M. C. Wyatt[1], G. M. Kennedy[1], D. J. Wilner[2], G. Duchene[3,5], A. M. Hughes[6], M. Pan[7], A. Shannon[1,8,9], M. Clampin[10], M. P. Fitzgerald[11], J. R. Graham[3], W. S. Holland[12], O. Panić[13], and K. Y. L. Su[14]

[1] Institute of Astronomy, University of Cambridge, Madingley Road, Cambridge CB3 0HA, UK; l.matra@ast.cam.ac.uk
[2] Harvard-Smithsonian Center for Astrophysics, 60 Garden Street, Cambridge, MA 02138, USA
[3] Astronomy Department, University of California, Berkeley CA 94720-3411, USA
[4] SETI Institute, Mountain View, CA 94043, USA
[5] Univ. Grenoble Alpes/CNRS, IPAG, F-38000 Grenoble, France
[6] Department of Astronomy, Van Vleck Observatory, Wesleyan University, 96 Foss Hill Dr., Middletown, CT 06459, USA
[7] MIT Department of Earth, Atmospheric, and Planetary Sciences, Cambridge, MA 02139, USA
[8] Department of Astronomy & Astrophysics, The Pennsylvania State University, State College, PA 16801, USA
[9] Center for Exoplanets and Habitable Worlds, The Pennsylvania State University, State College, PA 16802, USA
[10] NASA Goddard Space Flight Center, Greenbelt, MD 20771, USA
[11] Department of Physics & Astronomy, University of California, Los Angeles, CA 90095, USA
[12] Astronomy Technology Centre, Royal Observatory Edinburgh, Blackford Hill, Edinburgh EH9 3HJ, UK
[13] School of Physics and Astronomy, University of Leeds, Woodhouse Lane, Leeds, LS2 9JT, UK
[14] Steward Observatory, University of Arizona, 933 North Cherry Avenue, Tucson, AZ 85721, USA

Abstract

Recent Atacama Large Millimeter/submillimeter Array observations present mounting evidence for the presence of exocometary gas released within Kuiper Belt analogs around nearby main-sequence stars. This represents a unique opportunity to study their ice reservoir at the younger ages when volatile delivery to planets is most likely to occur. We here present the detection of CO $J = 2$-1 emission colocated with dust emission from the cometary belt in the 440 Myr old Fomalhaut system. Through spectrospatial filtering, we achieve a 5.4σ detection and determine that the ring's sky-projected rotation axis matches that of the star. The CO mass derived ($(0.65$–$42) \times 10^{-7}\,M_{\oplus}$) is the lowest of any circumstellar disk detected to date and must be of exocometary origin. Using a steady-state model, we estimate the CO+CO$_2$ mass fraction of exocomets around Fomalhaut to be between 4.6% and 76%, consistent with solar system comets and the two other belts known to host exocometary gas. This is the first indication of a similarity in cometary compositions across planetary systems that may be linked to their formation scenario and is consistent with direct interstellar medium inheritance. In addition, we find tentative evidence that (49 ± 27)% of the detected flux originates from a region near the eccentric belt's pericenter. If confirmed, the latter may be explained through a recent impact event or CO pericenter glow due to exocometary release within a steady-state collisional cascade. In the latter scenario, we show how the azimuthal dependence of the CO release rate leads to asymmetries in gas observations of eccentric exocometary belts.

Key words: circumstellar matter – comets: general – molecular processes – planetary systems – stars: individual (Fomalhaut A) – submillimeter: planetary systems

1. Introduction

Icy comets originating from the Kuiper Belt or the Oort cloud are believed to be the most pristine bodies in our own solar system, relics of the environment where the planets formed and evolved (see Mumma & Charnley 2011, and references therein). The unambiguous detection of exocometary volatiles in extrasolar debris disks, young Kuiper Belt analogs around main-sequence stars, has recently given us the opportunity to expand such compositional studies to planetary systems beyond our own. Crucially, these volatile-bearing systems are observed at a very dynamically active phase of evolution (ages of about tens of megayears), when terrestrial planet formation is at its final stages and volatile delivery is most likely to take place (Morbidelli et al. 2012, and references therein). Moreover, a comparison of volatile compositions in systems across a range of ages and host-star properties may yield important clues on the formation of these belts within the protoplanetary disk (for a review, see Wyatt et al. 2015).

Compositional studies of volatiles in exocometary belts have been carried out in terms of elemental abundances from observations of daughter atomic species (as done in β Pictoris, e.g., Roberge et al. 2006; Brandeker et al. 2016). In addition, metallic gas originating from sublimation or collisional evaporation of refractory elements has been detected and characterized in a few systems (e.g., Redfield 2007; Nilsson et al. 2012; Hales et al. 2017). More recently, we have also been able to use observations of CO gas emission at millimeter wavelengths, where this is likely produced either as a parent molecule or through the photodestruction of CO$_2$ (Dent et al. 2014; Matrà et al. 2015, 2017; Marino et al. 2016). While detection of exocometary parent molecules is the most direct route to the composition of exocometary ices, it is challenging due to the generally short survival timescale of gas molecules against stellar and interstellar UV photodissociation. This means that detection (so far limited to the CO molecule) has only been achievable with the extreme increase in sensitivity brought by the Atacama Large Millimeter/submillimeter Array (ALMA). On the other hand, atomic daughter products from molecular photodestruction are long-lasting (e.g., Fernández et al. 2006; Brandeker 2011; Kral et al. 2017) and may viscously expand over time to form an

atom-dominated accretion disk, a picture that is consistent with all far-infrared and millimeter observations of exocometary gas in the β Pictoris system to date (Kral et al. 2016).

The nearby (7.7 pc, van Leeuwen 2007), 440 ± 40 Myr old (Mamajek 2012), A3V (Gray & Garrison 1989) star Fomalhaut is the 18th brightest star at visible wavelengths beyond our own Sun. The star hosts a planetesimal belt producing dust first detected through its excess emission above the stellar photosphere at infrared wavelengths (e.g., Aumann 1985) and later imaged in thermal (Holland et al. 1998, 2003) and scattered (Kalas et al. 2005, 2013) light. These revealed that the belt is confined to a ring of $\sim$15 au width at a distance of $\sim$140 au from the star, and that it has a significant eccentricity of $\sim$0.1. The latter causes pericenter glow at infrared wavelengths, due to material being significantly closer to the central star with respect to the apocenter, causing it to be hotter and brighter (Wyatt et al. 1999; Stapelfeldt et al. 2004; Marsh et al. 2005; Acke et al. 2012). This eccentricity and the sharpness of the belt's inner edge were attributed to a shepherding planet-mass companion (Kalas et al. 2005). The subsequent *Hubble Space Telescope* (*HST*) discovery of the very low mass companion Fomalhaut b (Kalas et al. 2008) appeared consistent with the hypothesis that a planet could sculpt the inner edge (Quillen 2006; Chiang et al. 2009), until further observations showed that Fomalhaut b's orbit is highly eccentric (Kalas et al. 2013; Beust et al. 2014; Pearce et al. 2015). The existence of Fomalhaut b has been independently replicated (Currie et al. 2012; Galicher et al. 2013), but its physical properties continue to be investigated (Marengo et al. 2009; Kennedy & Wyatt 2011; Janson et al. 2012, 2015; Kenyon et al. 2014; Tamayo 2014; Kenyon & Bromley 2015; Lawler et al. 2015; Neuhäuser et al. 2015).

ALMA 850 μm imaging of part of the belt (near the northwest (NW) ansa) confirmed the steepness of the inner and outer edge of the parent body distribution (Boley et al. 2012). Further, higher resolution 1.3 mm imaging (White et al. 2017), though only covering the region along the ring's minor axis, tightened the constraints on the ring's width, as well as confirming the slope of the size distribution previously obtained through Australian Telescope Compact Array 7 mm observations (Ricci et al. 2012). However, only complete millimeter imaging of the ring can constrain its azimuthal morphology and eccentricity. We achieved the latter through a new 1.3 mm mosaic obtained with ALMA and described in MacGregor et al. (2017); in particular, we confirm that the geometry of the parent body ring resembles that of the smaller grains, and we achieve the first conclusive detection of apocenter glow, caused by the higher surface density expected at apocenter with respect to pericenter, due to particles on eccentric orbits spending more time at apocenter (Pan et al. 2016).

In parallel to the latest observations of the dust ring, recent deep searches for molecular CO $J = 3$-2 emission around the belt's NW ansa at 345 GHz with ALMA (Matrà et al. 2015), as well as searches for atomic ionized carbon (C II) and neutral oxygen (O I) through far-infrared *Herschel* spectroscopy (Cataldi et al. 2015), yielded null results. The CO nondetection was used to set an upper limit to the CO ice content in the planetesimals, but this was still consistent with (and close to the upper boundary of) the range of CO abundances observed in solar system comets. On the other hand, the nondetection of atomic gas, tracing the bulk of the gas in an exocometary origin

scenario, was used to derive a low upper limit to the gas/dust ratio; being well below 1, this ruled out gas–dust interactions as the origin for the narrow eccentric ring in the Fomalhaut system.

In this work, we present deeper ALMA CO $J = 2$-1 observations of the entirety of the Fomalhaut belt, yielding the first detection of gas in the system. In Section 2 we describe the observations, focusing on the CO imaging procedure. A description of the detection through the spectrospatial filtering technique first applied in Matrà et al. (2015) is in Sections 3.1 and 3.2, followed by the constraints this detection sets on the ring's rotation axis (Section 3.2) and total CO mass (Section 3.3) and the consistency of the detection with the previous observation of the CO $J = 3$-2 transition (Section 3.4). Finally, we analyze the radial and azimuthal morphology of the CO emission (Section 3.5).

We then go on to discuss the implications of this result, including proving the exocometary origin of the gas (Sections 4.1–4.3), drawing the first comparison between the ice content of extrasolar and solar system comets (Section 4.4), and discussing the possible origin of the observed similarity with a particular emphasis on interstellar medium (ISM) volatile inheritance (Section 4.5). At the same time, we investigate the possible cause of the tentative CO enhancement observed at the belt's pericenter, focusing on a general prediction of CO pericenter or apocenter glow in eccentric exocometary belts such as Fomalhaut (Section 4.6). We conclude by summarizing the outcomes of this study in Section 5.

2. Observations

We observed the Fomalhaut belt with the ALMA array using Band 6 receivers, allowing simultaneously a wide bandwidth for 1.3 mm dust continuum imaging and a native spectral resolution of 1.27 km s^{-1} around the rest frequency of the CO $J = 2$-1 transition (230.538 GHz). The observational setup and the calibration, data reduction, and continuum imaging processes are described in detail in MacGregor et al. (2017). Within the spectral window containing the CO line, we carried out continuum subtraction on the combined visibility data set using the `uvcontsub` task within the CASA software package (version 4.5.2, McMullin et al. 2007). We image the visibility data set using the CLEAN task. We do not apply any image deconvolution, but carry out our analysis (next section) on the primary beam-corrected dirty CO data cube. To enhance detectability of low CO surface brightness, we apply a taper within CLEAN to achieve an imaging resolution that better matches the width of the ring ($2\rlap{.}''36 \times 2\rlap{.}''13$, as opposed to the $1\rlap{.}''52 \times 1\rlap{.}''12$ resolution achieved from natural visibility weights). These imaging steps should not affect our results significantly compared to using the visibilities directly, since our u-v coverage yields a well-behaved dirty beam with little sidelobe emission, never above the $\sim$4% level. Our final data cube has a root mean square (rms) noise level of 0.7 mJy beam^{-1} in a 1.3 km s^{-1} channel for a beam size of 18.2×16.4 au at the distance of the Fomalhaut system. The expected systematic flux calibration accuracy is of order $\sim$10% (Fomalont et al. 2014).
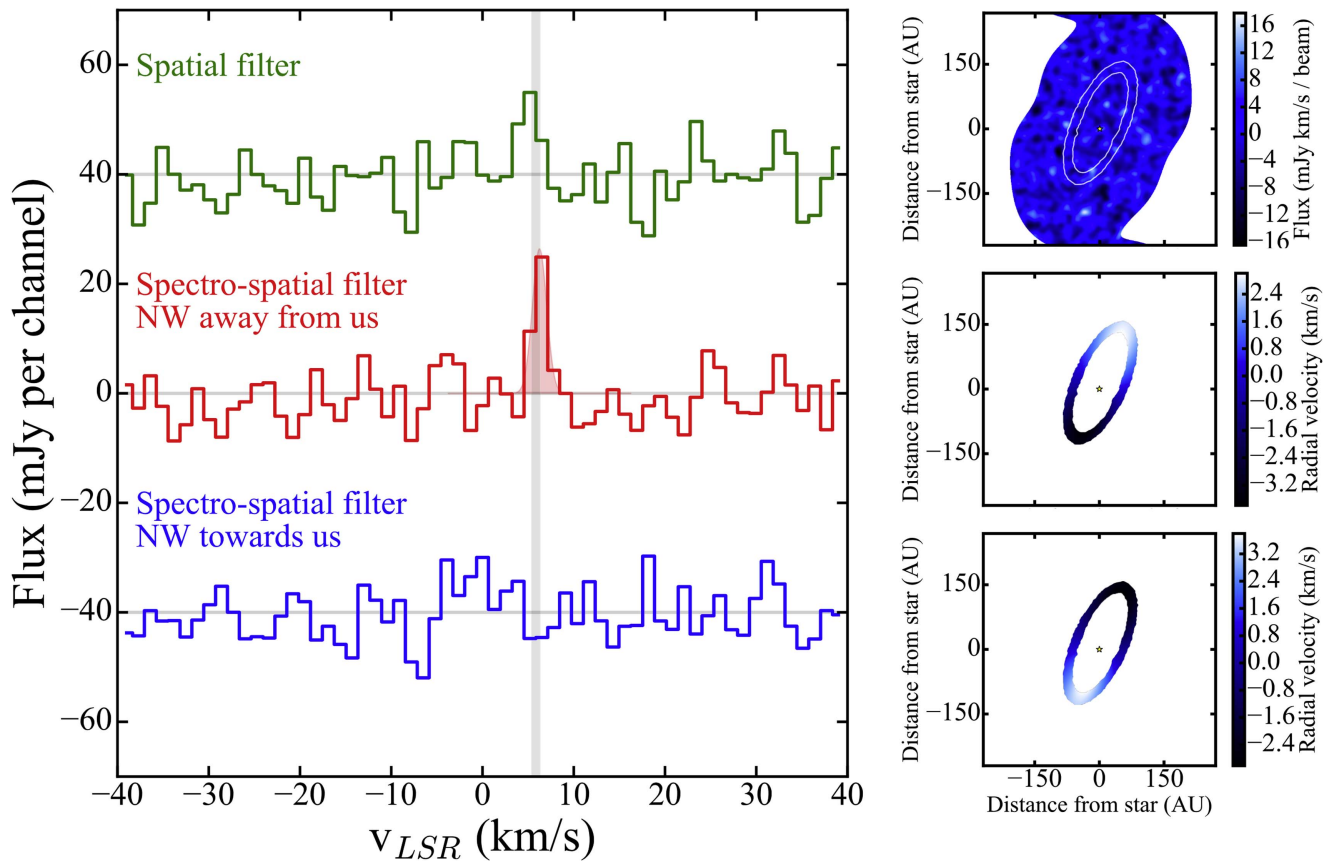
Figure 1. CO J = 2-1 ($\nu_{\rm rest}$ = 230.538 GHz) spectra of the Fomalhaut system obtained using different filtering techniques to achieve maximum S/N. Top: spectrum obtained through a spatial filter, by spatially integrating emission over the area where the dust continuum from the ring is detected at a level $>4\sigma$ (shown by contours overlaid on the moment-0 image displayed on the right). Center: spectrum obtained by applying a spectrospatial filter. The same spatial filter as above is applied after shifting the 1D spectrum at each spatial location by an amount equal to the opposite of its expected Keplerian radial velocity (see corresponding velocity map on the right). Bottom: spectrum obtained by applying the same spectrospatial filter, but assuming a reversed velocity field, with the NW ansa coming toward us (again, see corresponding velocity map on the right). A 3.3σ peak at a velocity consistent with that of the star (gray shaded region) is obtained using the spatial filter (top) and is boosted to 5.4σ using the spectral filter with the NW ansa moving away from us (center). The red shaded region is the spectrally unresolved Gaussian that best fits the filtered data.

3. Results and Analysis

3.1. Spatial Filter: CO J = 2-1 Detection

Figure 1 (top right) shows the CO J = 2-1 moment-0 map of the Fomalhaut ring, spectrally integrated within ± 3.5 km s^{-1} around the expected radial velocity of the star ($v_{\star,\rm LSR}$ = 5.8 $\pm$ 0.5 km s^{-1}; Gontcharov 2006). No statistically significant emission is observed above a noise distribution that is well approximated by a Gaussian and that has an rms of 4 mJy km s^{-1} beam^{-1}. The few 3–4σ peaks observed are in line with the expectation from the Gaussian noise distribution and the large number of resolution elements in the image. The contour lines indicate the sky region where continuum emission is detected above the 4σ level (MacGregor et al. 2017), corresponding to an area comprising a number of beams of $N_{\rm beams} \sim 40$. As done for previous Band 7 CO observations of the Fomalhaut system (Matrà et al. 2015), we now proceed by assuming that any CO present in the system should be of secondary origin and colocated with the dust from which it is produced, and later on we test these assumptions (Sections 3.5 and 4.1). This allows us to apply a spatial filter, that is, to spatially integrate the CO data cube over this region where the continuum is detected, yielding an improvement on the signal-to-noise ratio (S/N) equal to $\sqrt{N_{\rm beams}} \sim 6.4$. The obtained 1D

spectrum, shown in Figure 1 (left), presents a 3.3σ peak at a velocity consistent with the expected $v_{\star,\rm LSR}$.

3.2. Spectral + Spatial Filter: S/N Boost and Kinematics

In order to test the robustness and improve the significance of the detection, we make the further assumption that the CO gas lies in a vertically flat disk in Keplerian rotation around a star of 1.92 $M_\odot$, with the same orbital parameters as the dust ring, obtained from dust continuum imaging (MacGregor et al. 2017) and consistent with scattered light imaging (Kalas et al. 2013). Then, for each pixel location ($x_{\rm sky}$, $y_{\rm sky}$), where (0, 0) is the accurately known location of the star (detected in the continuum data set), we can determine the expected radial velocity field $v_z(x_{\rm sky}, y_{\rm sky})$ of the gas, both for the case in which the NW ansa is moving away from us (Figure 1, center right) or toward us (Figure 1, bottom right). Using this predicted velocity field, we apply a spectral filter; that is we shift the 1D spectrum at each ($x_{\rm sky}$, $y_{\rm sky}$) pixel location by $-v_z(x_{\rm sky}, y_{\rm sky})$, moving any CO emission from the predicted disk velocity to the stellar velocity $v_{\star,\rm LSR}$. If we then sum together the contributions from all pixels where the dust continuum is detected (or in other words, if we apply the spatial filter), we obtain a spectrum that is free from noise originating from spectral channels as well as spatial locations where no CO

emission is expected. As shown in Figure 1 (center left, for the velocity field in center right), this method boosts the S/N of the peak to 5.4σ.

The spectral filter yields kinematic information on the orbiting gas, since the S/N of the CO line is maximized only for the correct velocity field. This is because, for an incorrect velocity field, the spectral filter spreads CO emission over a larger number of velocity channels, reducing the S/N (see Figure 1, bottom left and right). This proves that CO gas in the NW ansa is moving away from us, while gas in the southeast (SE) ansa is coming toward us (Figure 1, center right). This is consistent with the kinematics of the star, whose SE part was also found to be moving toward us (Le Bouquin et al. 2009). We note that this information is still insufficient to derive the sense of rotation of the ring on-sky (clockwise or counter-clockwise), and in turn which side of the ring is closer to Earth and forward scattering (see discussion in Min et al. 2010; Kalas et al. 2013). This is because both the star and the CO only inform us on the sky-projected rotation axis, which is perpendicular to the sky-projected major axis of the ring and points in the northeast (NE) direction. However, the crucial missing piece of information is whether the ring's rotation axis is pointing toward us (i.e., inclination of $\sim+65°$ to the plane of the sky) or away from us ($\sim-65°$ inclination). Therefore, the current data are insufficient to determine whether the ring is rotating in a clockwise or counterclockwise direction on-sky, and whether the brighter NE side observed by *HST* is in front of or behind the sky plane.

3.3. Total Flux and CO Mass

In order to measure the integrated CO J = 2-1 line flux and the velocity centroid, we fit a Gaussian to the spectrospatially filtered spectrum derived above and shown in Figure 1 (center left). The best-fit Gaussian width is consistent with the line being unresolved, as expected from the application of our filtering method, and the best-fit velocity is $6.1 \pm 0.2 \, \mathrm{km \, s^{-1}}$, consistent with the expected stellar velocity of $5.8 \pm 0.5 \, \mathrm{km \, s^{-1}}$. The best-fit integrated line flux is $68 \pm 16 \, \mathrm{mJy \, km \, s^{-1}}$ (including the absolute flux calibration uncertainty, added in quadrature to the uncertainty from the Gaussian fit), or $(5.2 \pm 1.2) \times 10^{-22} \, \mathrm{W m^{-2}}$.

Assuming that the CO is optically thin to the line of sight at the observed frequency (which we verify in the next paragraph), we use a nonlocal thermodynamic equilibrium molecular excitation analysis (Matrà et al. 2015) to derive constraints on the total CO mass in the system. The derived mass value depends on two unknown parameters, the kinetic temperature of the gas and the density of the main collisional partners. We take the main colliders to be electrons, since these are most likely to be the dominant species for which CO collision rates are known if the gas is of exocometary origin (Matrà et al. 2015). We cover the full electron density parameter space between the radiation-dominated and local thermodynamic equilibrium regimes, and we probe a wide range of kinetic temperatures between 10 and 1000 K. The CO mass derived is in the range $(0.65-42) \times 10^{-7} \, M_{\oplus}$, where the boundaries were obtained from the $\pm 1\sigma$ limits on the integrated line flux. This is the lowest CO mass detected in any circumstellar disk to date, which is readily understood by noting that Fomalhaut, at a distance of 7.7 pc, is the nearest circumstellar disk where CO has been searched for by ALMA

to date. We will discuss the implication of this mass measurement in Section 4.1.

We note that the CO excitation model does not yet account for the effect of infrared or UV pumping, that is, transitions between vibrational and electronic levels within the molecule. These are excited in the presence of a strong infrared or UV radiation field, as may be the case around an A star such as Fomalhaut. As molecules relax to the ground electronic or vibrational levels, higher rotational levels may be more populated than predicted through CMB radiation alone, affecting the rotational level populations. Nonetheless, this would only influence the molecule in the radiation-dominated regime, or in other words it would only change our upper limit on the derived range of CO masses. Since less mass would be needed to produce the same flux in the presence of significant UV/IR pumping, our derived CO mass range can be taken as a conservative estimate and is likely narrower than derived above.

We now carry out a check to probe the optical thickness of the CO line. We assume that the CO density is uniform in a disk with inner radius at $R = 136.3$ au and $\Delta R = 13.5$ au wide, with a constant aspect ratio $h = H/R$ (height above the midplane divided by the radius) equal to the best-fit mean proper eccentricity of the planetesimals from continuum observations (0.06, MacGregor et al. 2017). This way, we can derive the ring volume and hence measure an average CO number density for our range of CO masses, obtaining a range of number densities in the range $(2-75) \times 10^{-2} \, \mathrm{cm^{-3}}$. We then estimate the maximum column density using the longest path length along the line of sight passing through our simple model ring described above. We neglect any column density enhancement expected at the two ansae due to projection effects (see Section 4.6). For the range of number densities above, this yields maximum column densities of $(0.04-1.67) \times 10^{14} \, \mathrm{cm^{-2}}$ for a maximum line-of-sight path length of ~ 15 au. Finally, we calculate the maximum optical thickness through its definition (Equation (3) in Matrà et al. 2017) for the full range of electron densities and kinetic temperatures probed above, and for an intrinsic line width taken to be equal to the Doppler broadening expected from each of the temperatures considered. The maximum, worst-case-scenario optical thickness we obtain is $\tau \lesssim 0.18$ (with values ranging down to 10^{-4} depending on the parameters), which confirms our optically thin assumption and our CO mass measurement.

3.4. Consistency with Archival Band 7 Observations

We now check that our detection of the CO J = 2-1 line is consistent with the CO J = 3-2 upper limit available from previous ALMA Band 7 observations (Matrà et al. 2015). For a well-characterized millimeter radiation field such as that around Fomalhaut (see Figure 3 in Matrà et al. 2015), line ratios of optically thin molecular transitions only depend on two free parameters determining the level populations of the upper level of each transition. These are the gas kinetic temperature T_k and the density of collisional partners n_{e^-}. Taking our J = 2-1 integrated line flux of $(5.2 \pm 1.2) \times 10^{-22} \, \mathrm{W m^{-2}}$ and the 3σ upper limit of $18 \times 10^{-22} \, \mathrm{W m^{-2}}$ on the J = 3-2 line flux from Matrà et al. (2015), we obtain an upper limit on the average 3-2/2-1 line ratio in the Fomalhaut ring of 3.5 or 6.7, depending on whether we consider our J = 2-1 measurement or its 3σ lower limit. This line ratio upper limit of 3.5 in
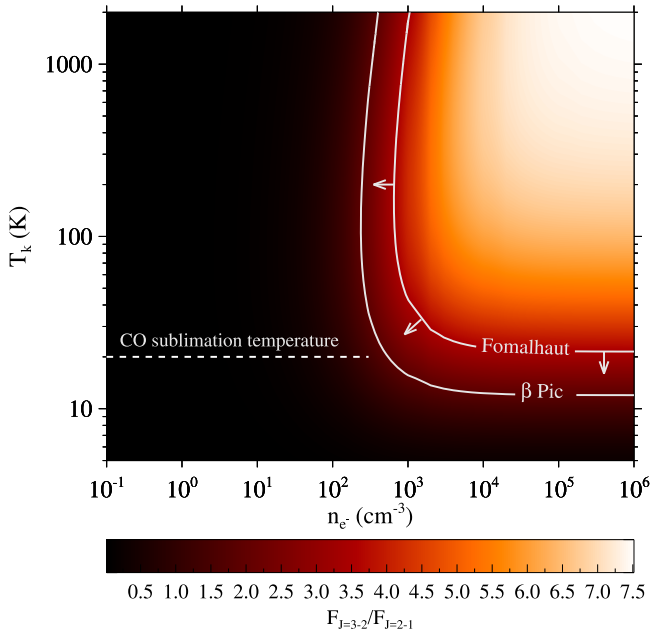
Figure 2. Color map of the CO $J = 3$-$2/J = 2$-1 line ratios expected for a wide range of kinetic temperatures T_k and electron densities n_{e^-}. The disk-averaged upper limit we estimate in the Fomalhaut belt is consistent with the value found for the β Pic disk, implying that similar excitation conditions in the two disks are still possible and explaining the CO $J = 3$-2 Fomalhaut nondetection in Matrà et al. (2015).

Fomalhaut will therefore trace a line in T_k–n_{e^-} space (Figure 2), the latter two quantities being degenerate. For comparison, we show the average line ratio measured in the β Pictoris disk (Matrà et al. 2017). While strictly speaking we can only exclude 3-2/2-1 line ratios higher than 6.7, we find that the archival nondetection of the $J = 3$-2 transition is in agreement with a β Pictoris-like gaseous environment (average line ratio of 1.9 ± 0.3) and fully consistent with the new $J = 2$-1 detection. While this is purely a consistency check, we remind the reader that there is no reason to assume that the electron density or CO excitation conditions in the Fomalhaut belt should be the same as around β Pictoris. Furthermore, we note once again that the introduction of UV/IR pumping in our model may influence Figure 2 by increasing the minimum possible line ratio in the radiation-dominated regime of excitation (left-hand side in the figure).

3.5. Radial and Azimuthal Morphology

In order to extract information on the spatial distribution of CO, we relax the assumption that it must be colocated with the dust millimeter continuum. In particular, we apply the spectral filter method to the entire data cube, shifting spectra in each spatial pixel to align CO emission with the stellar velocity. Instead of spatially integrating across the area where the continuum is detected, we examine the channel map corresponding to the stellar velocity (as shown in Figure 3). As expected, due to spatial dilution of the emission, no obvious significant emission is seen along the whole dust ring. For a given semimajor axis in the ring's orbital plane, taking once again the orbital parameters from dust continuum fitting, we can obtain a sky-projected orbit, and we average all azimuthal contributions along it to obtain an intensity profile as a function of ring semimajor axis. The black line in Figure 4 shows the semimajor axis profile between 50 and 220 au obtained by
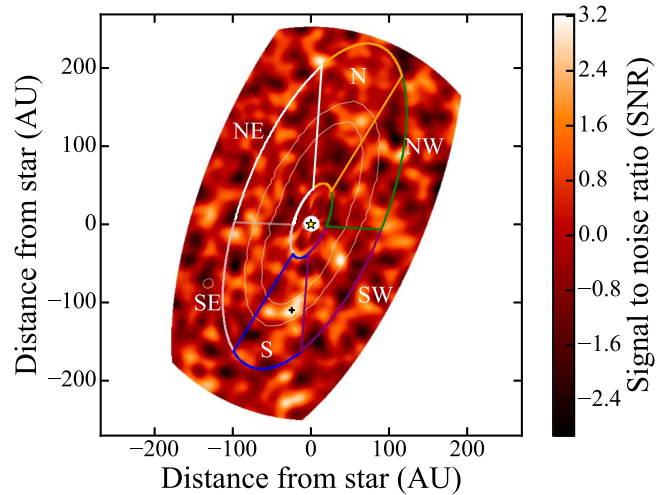

Figure 3. The color scale shows the CO S/N map obtained after spectral filtering. For each pixel, given some orbital parameters (see main text), emission from the velocity channel corresponding to the expected Keplerian velocity is shown. The thin white contours represent regions where the dust continuum is detected above the 4σ level. Wedges of different colors represent regions used to obtain the radial profiles displayed through the same colors in Figure 4. A significant enhancement is seen in the southern (S) wedge and is located near the best-fit pericenter location (plus sign) as determined from ALMA dust continuum imaging (MacGregor et al. 2017).
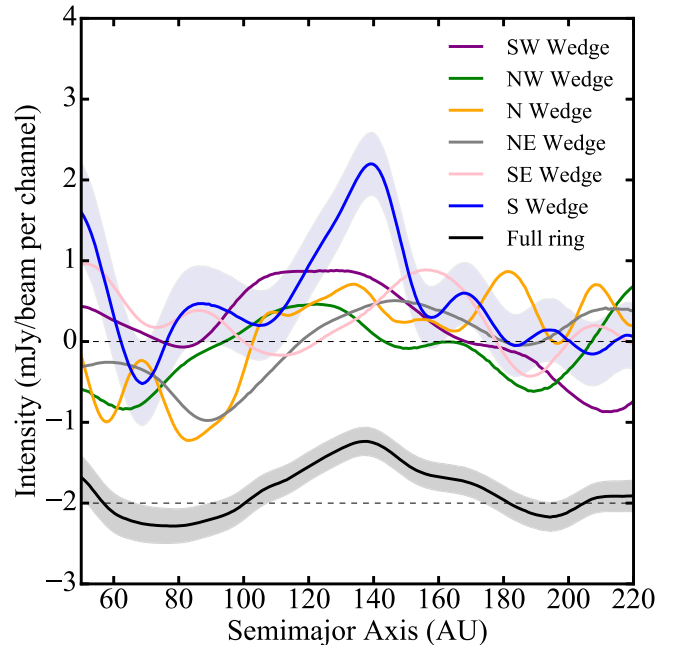
Figure 4. Radial profiles obtained through azimuthal averaging of the spectrally filtered CO map. Lines of different colors show profiles averaged within each of the wedges in Figure 3. The blue shaded region represents the $\pm 1\sigma$ confidence interval as a function of radius within the south wedge. This interval is similar for other wedges, not shown for clarity. The black line and gray shaded region (shifted vertically by -2 mJy beam^{-1} per channel) are the same profile and confidence interval obtained through azimuthal averaging over all azimuths.

azimuthally averaging around all true anomalies, showing a CO detection at the semimajor axis and width consistent with the dust continuum ring. This confirms that CO is indeed colocated with dust in the Fomalhaut belt.

Finally, we test for any indication of azimuthal asymmetry in the CO emission. To begin with, we construct the same
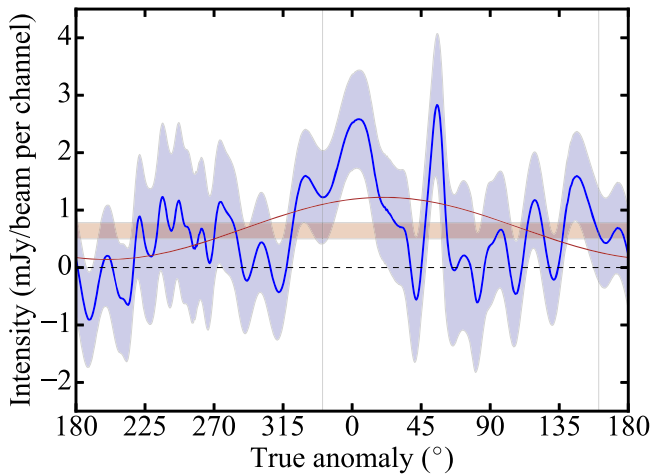
Figure 5. Radially integrated intensity between 120 and 150 au (blue line) as a function of true anomaly from the spectrally filtered CO map in Figure 3. The shaded region represents the $\pm 1\sigma$ confidence interval. The red line is the cosine function that best fits the data; the red shaded region is the $\pm 1\sigma$ interval of its best-fit mean, confirming our detection. The vertical thin gray lines are the locations of the on-sky ansae.

semimajor axis profile for each of six azimuthal regions, or "wedges," as displayed through different colors in Figure 3. These profiles are shown by the corresponding colors in Figure 4. For a perfectly axisymmetric on-sky surface brightness distribution of the ring, due to averaging across only about one-sixth of the azimuths, we expect the S/N in each wedge to decrease by a factor of $\sim\sqrt{6} = 2.45$ compared to the profile averaged across all azimuths and to lie at the $1-2\sigma$ level. However, the majority of CO emission appears to originate from the south (S) wedge (blue), where CO is detected at the 6.2σ level. The latter is also apparent in Figure 3, where we see that this region of emission is located near the ring's pericenter location, as determined by ALMA dust continuum fitting ($\omega = 22^\circ.5 \pm 4^\circ.3$, black cross in Figure 3; MacGregor et al. 2017). We find that the flux in the S wedge contributes to $(49 \pm 27)\%$ of the flux integrated across all azimuths; given the low S/N levels, we cannot distinguish whether all of the emission originates from this wedge or whether other regions also contain CO emission, as however hinted at by the low levels of positive emission observed across all wedges.

To analyze this azimuthal variation in more detail, Figure 5 shows the azimuthal profile obtained by integrating emission between semimajor axes of 120 and 150 au for all true anomalies f. We recover the enhancement at pericenter (true anomaly $f = 0^\circ$) and another 2.6σ peak of emission at $f \sim 45^\circ$, also evident in Figure 3. We then fit a cosine function to this azimuthal profile; this is a good representation of the expectation from our steady-state release model discussed in Section 4.3, for the case where a pericenter enhancement of the CO mass with respect to apocenter is predicted. We use Levenberg–Marquardt least-squares minimization to find the best-fit phase, mean intensity, and pericenter-to-apocenter intensity enhancement ($1 - I_{\rm apo}/I_{\rm peri}$) of our model cosine function. The phase obtained with respect to pericenter ($20^\circ \pm 25^\circ$) is consistent with the model having a maximum near pericenter. The mean (0.68 ± 0.16 mJy beam^{-1} per 1.3 km s^{-1} channel) being significantly different from zero is further confirmation of our detection at a level consistent with the radial profile in Figure 4, bottom, and with the spectrum in Figure 1, center left. This cosine fit leads to an

estimate of a pericenter enhancement with respect to apocenter of $(88 \pm 25)\%$. We will compare such an enhancement to model predictions in Section 4.6.

4. Discussion

Through spectral and spatial filtering applied to new ALMA observations, we detected low levels of CO $J = 2\text{-}1$ emission colocated with dust in the Fomalhaut ring, and we measured the CO gas mass to be between 0.65 and $42 \times 10^{-7} \, M_\oplus$. We then used line velocities to show that the ring's sky-projected rotation axis points to the NE, matching that of the star; in other words, the SE ansa is moving toward us, and the NW away from us. Finally, we presented tentative evidence that most of the detected emission originates near the ring's pericenter, as determined by our fitting of the ALMA dust continuum image (MacGregor et al. 2017).

In this section, we investigate the origin of the CO observed, proving its exocometary nature and discussing its origin in either a recent impact or a steady-state release. Then, we use a steady-state collisional cascade model to derive exocometary ice compositions. This allows us to compare Fomalhaut with other planetary systems, including the solar system, and to make the prediction of CO pericenter or apocenter glow in eccentric exocometary rings.

4.1. The Exocometary Nature of the Gas

The origin of gas remains to be found for most of the known gas-bearing debris disks. A primordial versus secondary origin dichotomy has emerged in the past years, due to the youth ($\lesssim 40$ Myr) of the detected systems (see Section 1). Aside from a tentative detection of CO emission in the 1–2 Gyr old η Corvi system (Marino et al. 2017), which is not colocated with the outer dust belt and remains to be confirmed, Fomalhaut is the most evolved debris belt to host CO gas, at an age of (440 ± 40) Myr.

Can the observed CO have survived since the protoplanetary phase of evolution? CO survival requires shielding from the interstellar UV radiation field, which otherwise rapidly photodissociates the molecule on a timescale $t_{\rm phd}$ of 120 years. This shielding can be produced by CO itself and other molecules such as H$_2$, where the latter dominates the gas mass in the primordial origin scenario. In Section 3.3, through a simplified model, we estimated an average number density of CO in the ring of order $(2–75) \times 10^{-2}$ cm^{-3}. In this model, a CO molecule sitting in the radial and vertical center of the ring will therefore have a CO column density of order $10^{12}–10^{14}$ cm^{-2} surrounding it and, assuming a low CO/H$_2$ abundance ratio of 10^{-6} (similar to that found in the old TW Hya protoplanetary disk; Favre et al. 2013), a H$_2$ column density of order $10^{18}–10^{20}$ cm^{-2}. Since these CO and H$_2$ column densities are insufficient to shield CO over the system's lifetime (Visser et al. 2009), we conclude that the observed CO cannot have survived since the protoplanetary phase. We note that freeze-out onto grains is also negligible, due to the relatively low density of grains in the ring and their temperature being much above the CO freeze-out temperature (Matrà et al. 2015). The observed CO must therefore be of secondary origin, that is, recently produced through either continuous, steady-state replenishment or a recent stochastic event. We analyze both possibilities below.

4.2. Origin of the Gas: Stochastic Collision

For a stochastic collision, the requirement is recent production of the observed CO mass, at least $6.5 \times 10^{-8} M_{\oplus}$. Assuming a 10% $CO+CO_2$ mass fraction, this requires the destruction of a comet of total mass $6.5 \times 10^{-7} M_{\oplus}$, or about 300 Hale–Bopp masses (e.g., Weissman 2007). Given the observationally well constrained mass loss rate of small grains through the collisional cascade (Appendix B) and the known CO mass and photodestruction rate (previous section), we can estimate (see next section) the collisional mass loss rate of such large, $CO+CO_2$-rich bodies in the cascade, obtaining a range of 0.012–$0.046 M_{\oplus} \, \mathrm{Myr}^{-1}$. Then, we can estimate that the time-scale for collisions between any such supercomets to take place is 14–54 years, meaning that the rate is 2.2–8.6 every 120 years (the survival timescale of CO). This would suggest that it is possible that the recent destruction of a large body within the belt, alone, produced all of the observed CO mass.

However, this conclusion is subject to the assumption that bodies of the required $6.5 \times 10^{-7} M_{\oplus}$ mass for CO release, which would be $\sim$100 km in size, lose mass at the same rate as other bodies participating in the collisional cascade. This implicitly assumes an extrapolation of the size distribution from small, observable grains up to bodies of this size. Although $\sim$100 km is consistent with observations of the Kuiper and asteroid belts in the solar system (Bottke et al. 2005; Fraser et al. 2014), as well as other planetesimal growth models (Johansen et al. 2015; Shannon et al. 2016), it remains to be determined whether such large bodies in the Fomalhaut belt exist and participate in the collisional cascade. If we extrapolate the power-law size distribution of Wyatt & Dent (2002) to large sizes ($n(D) \propto D^{2-3q}$ with $q = 11/6$, Figure 8 in their paper), we find that there should be 7×10^7 objects with this or larger mass within the Fomalhaut ring. Then, the collision timescale of one supercomet is $\sim$1.0–3.8 Gyr, which is longer than the $\sim$440 Myr age of the system. This indicates supercomets would have seldom collided over the age of the system, and their size distribution would therefore have been set by growth processes during planet formation, where the latter is completely unconstrained observationally. In addition, if the extrapolation of the size distribution to these sizes were valid, the total mass of the belt ($\sim$0.4 Jupiter masses) would be $\sim$4 times higher than the $29 M_{\oplus}$ that an initial minimum-mass solar nebula (MMSN) planetesimal disk would have had between 120 and 150 au (Kenyon & Bromley 2008). In general, these required high belt masses challenge the validity of our extrapolation and point to a likely steeper size distribution for the large primordial bodies (as is the case for Kuiper Belt objects, e.g., Schlichting et al. 2013).

Overall, this caveat would make our estimated high collision rate for large bodies an upper limit. To conclude, it is therefore possible that the destruction of a large icy body released all the CO observed in the Fomalhaut ring, although a reasonable likelihood for this event to happen requires the Fomalhaut belt to be massive, of order of a few times higher than the expectation from an MMSN-like disk.

4.3. Origin of the Gas: Steady-state Release and Ice Composition

On the other hand, we can consider the total gas release expected from the steady-state collisional cascade in the framework described in Matrà et al. (2015) and already applied

to other debris disks hosting secondary gas (see Section 4.4). Regardless of the details of the ice-removal mechanism, this method can be used to estimate the $CO+CO_2$ ice mass fraction in Fomalhaut's exocomets that is required to produce the observed CO gas. In summary, we assume that a steady-state collisional cascade is in place within the ring, with large parent bodies grinding down to produce dust of sizes all the way down to the blow-out limit (e.g., Wyatt & Dent 2002).

Solid mass is being inputted through catastrophic collisions of the largest comets in the collisional cascade, and the CO $+CO_2$ mass fraction will be lost through gas release within the cascade. The condition of steady state imposes that the rate at which mass is being inputted by the largest bodies ($\dot{M}_{D_{\max}}$) is equal to the sum of the rate at which mass is being lost through $CO+CO_2$ outgassing ($\dot{M}_{CO+CO_2}$) and the rate at which mass is being lost through radiation forces at the bottom of the cascade, $\dot{M}_{D_{\min}}$. Assuming that all of the $CO+CO_2$ ice is lost through the cascade before reaching the smallest-sized grains (see discussion in next section), we have $\dot{M}_{CO+CO_2} = f_{CO+CO_2} \dot{M}_{D_{\max}}$, meaning that we can measure the $CO+CO_2$ ice mass fraction in exocomets f_{CO+CO_2} through

$$f_{CO+CO_2} = \frac{1}{1 + \dot{M}_{D_{\min}}/\dot{M}_{CO+CO_2}}. \qquad (1)$$

In a steady state, the outgassing rate of $CO+CO_2$ molecules equals their destruction rate (where the latter is known) through $\dot{M}_{CO+CO_2} = M_{CO \, obs}/t_{phd}$. Additionally, the mass loss rate $\dot{M}_{D_{\min}}$ of $CO+CO_2$-free particles at the small size end of the collisional cascade can be estimated by considering the collision timescale of particles just above the minimum size in the distribution (Appendix B). The latter is well constrained by observations and can be calculated as shown in Equation (21).

Overall, the $CO+CO_2$ ice mass fraction of exocomets can therefore be estimated through

$$f_{CO+CO_2} = \frac{1}{1 + 0.0012 \, R^{1.5} \Delta R^{-1} f^2 L_{\star} M_{\star}^{-0.5} t_{phd} M_{CO \, obs}^{-1}}, \qquad (2)$$

where R and ΔR are in au, $L_{\star}$ and $M_{\star}$ are in $L_{\odot}$ and $M_{\odot}$, t_{phd} is in years, and $M_{CO \, obs}$ in $M_{\oplus}$. The $CO+CO_2$ ice mass fraction in Fomalhaut is therefore in the range 4.6%–76% (taking the observed belt parameters quoted in Appendix B).

4.4. Comparison with Other CO-bearing Systems: An Overall Similarity to Solar System Comets

Our compositional measurement in exocomets within the Fomalhaut ring adds to the other two measurements of the CO $+CO_2$ exocometary ice mass fraction obtained through ALMA observations of second-generation CO gas, β Pictoris (Matrà et al. 2017) and HD 181327 (Marino et al. 2016). For consistency, we also apply our updated, more accurate estimation of the ice mass fraction presented here to these systems, using the same belt and stellar parameters as in the original works. We find that the $CO+CO_2$ ice mass fraction becomes <32% for β Pictoris (using the 3σ upper limit on the CO mass) and in the range 0.8%–3.7% for HD 181327 (using the $\pm 1\sigma$ range of the CO mass). These two systems both belong to the β Pic moving group at an estimated age of 23 ± 3 Myr (Mamajek & Bell 2014) and are much younger than Fomalhaut, but they nonetheless present compositions that are within an order of magnitude of one another (Figure 6). For
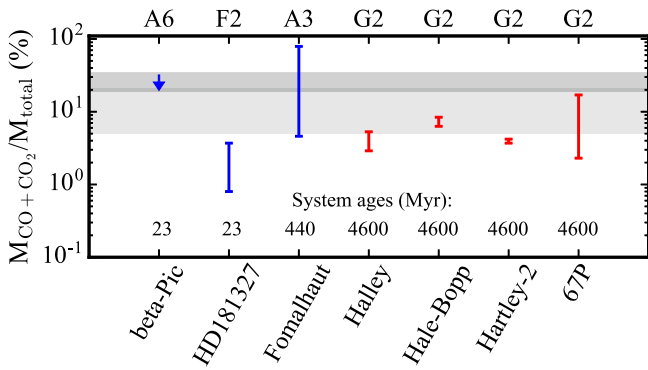
Figure 6. $CO+CO_2$ mass fraction (%) in solar system comets where both measurements are present (red, assuming a dust-to-ice ratio of ~4 as measured in comet 67P; Rotundi et al. 2015) and in exocometary belts observed so far (blue, derived in the steady-state framework). The tick labels on the top x axis indicate the spectral type of the host star. Compositions were derived from Matrà et al. (2017) (β Pic), Marino et al. (2016) (HD 181327), this work (Fomalhaut), and Le Roy et al. (2015) and references therein for solar system comets. Shaded regions represent the ranges of mass fractions expected from direct inheritance of ISM compositions (assuming 100% CO trapping within comets and no grain surface chemistry), in the cases where comets formed outside (darker gray) or inside (lighter gray) the CO ice line within the protoplanetary disk.

example, the weak detection in Fomalhaut compared to β Pic is easily explained by the fact that Fomalhaut is much less collisionally active. Indeed, the mass loss rate through the cascade is $\gtrsim20$ times higher for the β Pictoris disk, and the higher amounts of CO also mean that some self-shielding takes place, increasing the photodissociation timescale by a factor of ~2.5 (Matrà et al. 2017). Overall, for the same $CO+CO_2$ ice content, this indicates that the CO gas mass would be at least 50 times higher in β Pic with respect to Fomalhaut, in agreement with the observations. On the other hand, we note that our new Fomalhaut measurement is at least marginally inconsistent with that in the HD 181327 debris ring, potentially suggesting an intrinsic difference in composition or gas release mechanism between these two systems.

Despite the rather large error bars on the measurements obtained so far, Figure 6 also shows that the $CO+CO_2$ mass fraction in exocomets is consistent with that of solar system comets. A caveat to keep in mind in this comparison is that mass fractions in solar system comets are derived from measurements of the relative abundance of CO and CO_2 compared to H_2O. On the other hand, their refractory-to-volatile mass ratio, required to derive the $CO+CO_2$ mass fraction, is only poorly (if at all) known, due to the difficulty in remote measurements of dust production rates. The only comet for which this is measured robustly in situ is comet 67P/Churyumov–Gerasimenko (67P), where the dust-to-ice mass ratio is 4 ± 2 in the coma (Rotundi et al. 2015) and consistent with (though not directly constrained by) density measurements of the interior of its nucleus (Pätzold et al. 2016). We therefore assumed all solar system comets to have an equal refractory-to-volatile mass ratio of 4, though note that this may be subject to scatter across comet families and individual objects.

Another underlying assumption is that we are using observation-based estimates of the gas production (outgassing) rates of CO and CO_2 (as well as H_2O for solar system comets) as a probe for their relative solid abundance; in other words, we are assuming that $CO+CO_2$ ice and refractories are removed at rates that reflect their internal composition. In solar system

comets, linking outgassing rates in the comae and nuclei abundances depends not only on a comet's distance from the star (as clearly seen, e.g., for Hale–Bopp; Biver et al. 2002), but also on its detailed thermal and structural properties (Marboeuf et al. 2012). However, CO/H_2O and CO_2/H_2O outgassing rate ratios are generally measured near a comet's perihelion, where the process is dominated by water sublimation, which carries along CO and CO_2 trapped within it. Then, for a comet with a mostly homogeneous composition and dominated by clathrates (as shown to hold for 67P; Luspay-Kuti et al. 2016), outgassing ratios are expected to be a good representation of its ice abundance (see, e.g., Marboeuf & Schmitt 2014).

As with solar system comets, our exocometary abundance derivation also assumes that CO and CO_2 ice, as well as refractories, are released at rates that reflect their composition; in the context of our steady-state model, this is valid as long as two conditions apply:

1. No CO or CO_2 is removed as ice by way of the smallest blow-out grains in the cascade, which is of order $\sim10\,\mu m$ in the Fomalhaut belt (though it can vary depending on grain composition). In other words, these ices are only removed as gas. This applies if ices are completely lost further up the collisional cascade, that is, if either the sublimation or photodesorption timescale is shorter than the collision timescale for grains larger than the blow-out size. Taking as an example a pure water ice grain 20 μm in size, the results of Grigorieva et al. (2007) can be used to show that its photodesorption timescale is $\sim13,700$ years. On the other hand, its collisional lifetime is $\sim4 \times 10^5$ years (Wyatt & Dent 2002), meaning that water ice cannot survive on the surface of grains at the bottom of the collisional cascade. A similar argument applies for a pure CO_2 ice grain, whose photodesorption timescale will be very similar to that of water, due to a similar photodesorption yield of $\sim10^{-3}$ molecules photon^{-1} (Grigorieva et al. 2007; Öberg et al. 2009).

   The next question is whether CO gas or CO_2 ice can remain trapped within refractories all the way down to the smallest sizes in the cascade. Due to its low sublimation temperature (~20 K), CO is trapped already in gas form at the blackbody temperature of a dust grain within the Fomalhaut belt (~48 K), and for small grains at the bottom of the cascade, it is likely to diffuse through the refractory layer. On the other hand, CO_2 has a higher sublimation temperature of ~80 K (Collings et al. 2004). The hottest grains will be those near the blow-out limit ($\sim10\,\mu m$), which will have a temperature close to that observed in the spectral energy distribution (SED, ~74 K; Kennedy & Wyatt 2014). Further heating is likely to take place through collisions themselves (e.g., with accelerated high-β grains, as proposed by Czechowski & Mann 2007), increasing the likelihood of CO_2 sublimation and subsequent release through diffusion. In conclusion, while further detailed modeling is necessary, we deem it very unlikely for any CO to be retained within grains down to the smallest sizes in the cascade, but on the other hand we cannot exclude that a fraction of CO_2 ice may instead be retained within a refractory mantle. The latter would cause an underestimate of the $CO+CO_2$ exocometary mass fractions presented here.

2. CO and CO_2 production is not dominated by resurfacing collisions, which preferentially occur for large bodies at the

top of the cascade (A. Bonsor et al. 2017, in preparation). These less energetic collisions, which are not taken into account in our model, can expose trapped volatiles as well as fresh surface ice that can then be rapidly lost through sublimation or photodesorption. This would produce more gas mass than predicted through catastrophic-only planetesimal collisions, meaning that our model would be overestimating the cometary $CO+CO_2$ ice mass fraction. If resurfacing collisions are the main driver for gas release, we expect most of this release to happen early in the lifetime of the belt, since it requires the big planetesimals (holding most of the CO mass) to only have been resurfaced rather than destroyed. However, we note that these large bodies may also be large enough to retain the released gas through an atmosphere, or they could lose dust as well as gas through drag (as observed in solar system comets). Overall, it remains to be established whether gas released through resurfacing collisions can dominate the released mass, though such a study is beyond the scope of this paper.

4.5. Possible Origins for This Similarity and Comparison to a Simple ISM Inheritance Model

We find that $CO+CO_2$ mass fractions in exocomets are similar to each other and are of the same order (within about an order of magnitude) as observed for solar system comets (Le Roy et al. 2015 and references therein). As shown in Figure 6, this similarity appears to apply around host stars of a range of ages and spectral types. In terms of distance to the host star, exocometary gas is observed at 50–220 au around an 8.7 $L_\odot$ star (β Pic, Matrà et al. 2017), ~81 au around a 3.3 $L_\odot$ star (HD 181327, Marino et al. 2016), and ~135 au around a 16.6 $L_\odot$ star (this work, stellar luminosity from SED fit in Kennedy & Wyatt 2014). Assuming blackbody-like bodies, the equilibrium temperature in these belts would be equivalent to distances of 17–75, 45, and 33 au from the Sun in the solar system, meaning that the temperature of these exocomets should be of the same order as observed for the solar system's comet reservoir in the Kuiper Belt (30–50 au; e.g., Stern & Colwell 1997). Then, similar compositions and temperature environments for comets may indicate similar comet-formation conditions in younger protoplanetary disks, including the solar nebula.

Another aspect to consider is whether these cometary fractions of mass locked in CO and CO_2 are globally representative of the chemical heritage from the ISM (see Pontoppidan et al. 2014 for an extensive discussion of such inheritance). In the ISM, we know that the [CO/H_2] abundance ratio in the gas is of order 10^{-4}, where H_2 dominates the gas mass, and the gas/dust ratio is of order ~100. This yields a $M_{CO\,gas,ISM}/M_{total,solids,ISM} \sim 14\%$. On the other hand, the CO abundance in ISM ices is in the range [CO/H_2O]$_{ice,ISM}$ ~ 9%–36% compared to H_2O (Mumma & Charnley 2011, and references therein). The CO_2 content is dominated by its ice phase (e.g., van Dishoeck et al. 1996), with a [CO_2/H_2O]$_{ice,ISM}$ abundance of ~15%–44% (again, see Mumma & Charnley 2011 and references therein). This means that ISM material that is accreted in the outer regions of the protoplanetary disk will contain $CO+CO_2$ already in the ice form, with $M_{CO_2\,ice,ISM}/M_{H_2O\,ice,ISM} \sim 0.51$–1.64, and CO in the gas form, with $M_{CO\,gas,ISM}/M_{total,solids,ISM} \sim 0.14$.

Given their present location, we assume that cometary belts formed in protoplanetary disks outside the H_2O and CO_2 ice lines. This means that without significant vertical and outward radial mixing, H_2O and CO_2 remained locked on the grains with ISM abundances, producing cometary CO_2/H_2O abundances representative of the ISM. For the CO content, however, we consider two possible scenarios, where comets formed either outside or inside the CO ice line. Outside the CO ice line, the freeze-out of CO from ISM gas will enhance the ice-phase $CO+CO_2$ abundance compared to the ISM value. This simple scenario would yield a total $CO+CO_2$ mass fraction in the comets given by

$$\left(\frac{M_{CO+CO_2,ice}}{M_{total,solids}}\right)_{comet} = \frac{(M_{CO+CO_2,ice})_{ISM} + (M_{CO,gas})_{ISM}}{(M_{total,solids})_{comet}} \quad (3)$$

where

$$\frac{(M_{CO+CO_2,ice})_{ISM}}{(M_{total,solids})_{comet}} = \frac{1}{1 + \left(\frac{M_{dust}}{M_{ice}}\right)_{comet}} \frac{1}{1 + \left(\frac{M_{CO+CO_2,ice}}{M_{H_2O,ice}}\right)^{-1}_{ISM}} \quad (4)$$

and

$$\frac{(M_{CO,gas})_{ISM}}{(M_{total,solids})_{comet}} = \frac{1}{1 + \left(\frac{M_{CO,gas}}{M_{total,solids}}\right)^{-1}_{ISM}}. \quad (5)$$

Given CO gas and $CO+CO_2$ ice abundances in the ISM, assuming a range of dust-to-ice ratios between the $\pm 1\sigma$ values measured in comet 67P, we obtain an expected $CO+CO_2$ cometary mass fraction of ~17%–33% (darker shaded region in Figure 6). The growth of grains to comet-sized bodies allows CO ice originally on grain mantles to become trapped in other ices and refractories; this ensures that CO (and thus the CO $+CO_2$ mass fraction derived) can be retained once the protoplanetary disk is dispersed and the CO ice line moves farther out than the cometary belt location.

In the second formation scenario, where the cometary belt formed inside the CO ice line in the protoplanetary disk, no extra CO from ISM-like gas would be incorporated in the ice phase; this would imply a $CO+CO_2$ cometary mass fraction of ~5%–21% (lighter shaded region in Figure 6). As well as assuming that all of the CO can remain trapped within other ices or refractories inside its ice line, this simplified evolutionary model ignores any grain surface chemistry, which is likely ongoing through the ISM, protoplanetary, and cometary phases of evolution. We expect that such chemistry will act to deplete the CO and CO_2 ice abundances, creating not only more complex volatiles (which are not dominant in cometary ice), but also organic refractories. Strictly speaking, we should therefore consider these ranges as upper limits to the $CO+CO_2$ cometary mass fractions derived in this ISM inheritance model.

While the large error bars in the solar system and exocometary measurements do not allow us to draw significant conclusions with regard to enhancement or depletion compared to ISM-inherited abundances, we show that such a comparison should be possible with increasingly accurate observations. For example, measuring the depletion of $CO+CO_2$ abundance with respect to ISM-inherited values would allow us to estimate the amount of CO or CO_2 that has been lost either due to

sublimation during or immediately after dispersal of the protoplanetary disk (due to consequent outward movement of the CO ice line location) or due to grain surface chemistry and production of more complex organics. As well as achieving more accurate measurements over a larger sample of exo- and solar system comets, pinpointing the formation location of cometary belts within the protoplanetary disk with respect to the CO ice line will be crucial in allowing us to distinguish between the two possible ranges of ISM-inherited abundances discussed above.

4.6. Pericenter/Apocenter Glow of CO Released from a Steady-state Collisional Cascade

In Section 3.5 we presented tentative evidence of an enhancement in CO emission near the planetesimal belt's pericenter. Here, we examine its possible physical origin in the framework of our steady-state model described in Section 4.3. Once again, we assume that the CO gas produced is a fraction of the solid mass lost as part of a steady-state collisional cascade, giving us access to the $CO+CO_2$ ice abundance. The total solid mass loss rate $\dot{M}(D)$ is calculated by multiplying the mass $M_{solid}(D)$ in any given size bin with the collision rate $R_{col}(D)$ of bodies in that size bin.

In Appendix A, we quantify how this mass loss rate within an eccentric cometary belt depends on the true anomaly f, for two possible regimes of grain sizes releasing CO. For the small grains, under the condition $D < D_{min}(0.5\, v_{rel}^2/Q_D^\star)^{1/3}$, we find that the collision rate is independent of the true anomaly; this in turn means that the mass loss rate should be enhanced at the apocenter due to the expected enhancement in solid mass at this location (due to particles spending more time there). For larger grains ($D > D_{min}(0.5\, v_{rel}^2/Q_D^\star)^{1/3}$), the azimuthal dependence of the mass loss rate is set by six parameters, namely the slope of the size distribution in the collisional cascade q, the mean proper eccentricity of material orbiting within the belt e_p, the stellar mass $M_\star$, the belt semimajor axis a, the forced eccentricity of the belt e_{frc}, and the specific incident energy required for a catastrophic collision, $Q_D^\star$. For the case of the Fomalhaut belt, we have observational constraints on $q \sim 1.83$ (Ricci et al. 2012, where we assume it to be independent of true anomaly), $M_\star \sim 1.92\, M_\odot$ (Mamajek 2012), $a \sim 136.3$ au, and $e_{frc} \sim 0.12$ (MacGregor et al. 2017), meaning that our only free parameters are the mean proper eccentricity e_p and the specific strength $Q_D^\star$ of the planetesimals. We can then quantify the fractional difference in mass loss rate at pericenter with respect to apocenter $(1 - \dot{M}(f = 180°)/\dot{M}(f = 0°))$ using Equations (12) and (13) in Appendix A, shown for a wide range of e_p and $Q_D^\star$ values in Figure 7.

As expected, for low proper eccentricities and high planetesimal strengths, the effect of a higher mass at apocenter dominates over the effect of easier collisional disruption at pericenter. Vice versa, for high proper eccentricities and low planetesimal strengths, we see a pericenter enhancement in the mass loss rate due to the effect of easier collisional disruption at pericenter dominating over the effect of having a higher mass at apocenter. The upper and lower horizontal asymptotes of the curves correspond to the limits $e_p \to 0$ and $e_p \to \infty$ as calculated by setting $e_{frc} = 0.12$ in Equations (14) and (15) (Appendix A) and are independent of both e_p and $Q_D^\star$. This implies a $\sim 15\%$ maximum pericenter-to-apocenter enhancement in the mass loss rate of the Fomalhaut belt. For the $\pm 1\sigma$ range of proper eccentricities derived from continuum imaging
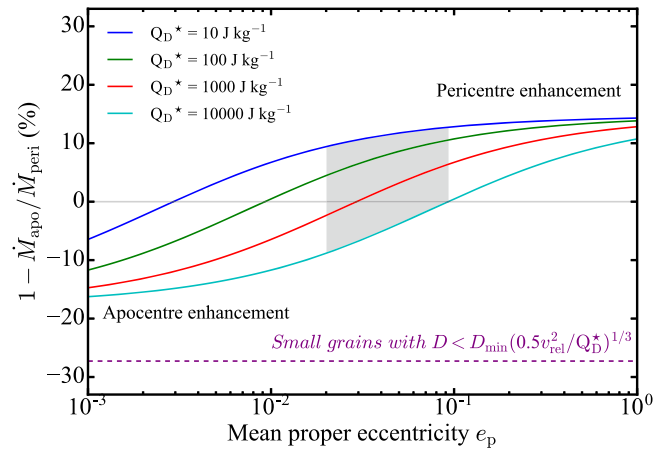

Figure 7. Solid mass loss rate (and hence CO mass) enhancement predicted at pericenter with respect to apocenter in the Fomalhaut ring, for CO released by small grains of sizes $D < D_{min}(0.5\, v_{rel}^2/Q_D^\star)^{1/3}$ (purple dashed line), or by larger grains of sizes $D > D_{min}(0.5\, v_{rel}^2/Q_D^\star)^{1/3}$ (colored solid lines). In the larger size regime, given the observationally constrained $M_\star$, q, a, e_{frc} (see text), the enhancement is only a function of the unknown proper eccentricity e_p of the planetesimals and of their threshold specific strength needed for catastrophic collisions $Q_D^\star$. The shaded region represents a wide range of $Q_D^\star$ as explored by Wyatt & Dent (2002) and the $\pm 1\sigma$ interval of e_p obtained from fitting the ALMA dust image (MacGregor et al. 2017).

(MacGregor et al. 2017) and $Q_D^\star$ values in the range 10–10,000 J kg^{-1}, expected for weak ice grains of a wide range of sizes within the collisional cascade (Wyatt & Dent 2002; assuming the results of Benz & Asphaug 1999), we predict the fractional difference in mass loss rate between pericenter and apocenter in the range -9% to 12%. Then, given that the CO photodissociation rate is independent of true anomaly, and assuming that the $CO+CO_2$ ice fraction is too, the steady-state mass loss rate enhancement at pericenter directly translates into a CO mass enhancement.

Whether a CO mass enhancement translates into a CO flux enhancement at pericenter/apocenter, or in other words CO pericenter/apocenter glow, also depends on the excitation of the CO molecule (see Section 3.4), and particularly on the radial dependence of the gas kinetic temperature and electron density. This is because for example in Fomalhaut, CO emitted at the ring's pericenter will be closer to the star than the CO at apocenter, by a factor of $(1 + e)/(1 - e) \sim 1.27$. Making the simple assumption of a β Pic-like environment for CO excitation, with an electron density varying with radius as $\sim 300(R/100\, \text{au})^{-1}\, \text{cm}^{-3}$ (Matrà et al. 2017), the expected flux at pericenter would be 2.5%–6.1% larger than that at apocenter, making the CO flux enhancement even larger than expected from a mass enhancement only. Therefore, we expect excitation effects to favor a CO flux enhancement at pericenter. We cautiously note that such a contribution from CO excitation will depend on the gaseous environment of the Fomalhaut belt; this may significantly differ from that of β Pic, though it may be characterized in the future using optically thin line ratio observations.

Finally, we need to take into account projection effects due to the viewing geometry; in particular, the observed pericenter-to-apocenter ratio will depend on the combined effect of the ring's vertical thickness, its inclination to the line of sight, and the on-sky angular distance between the ring's pericenter and the nearest ansa. This is because the azimuthal intensity distribution for a significantly inclined ring with a
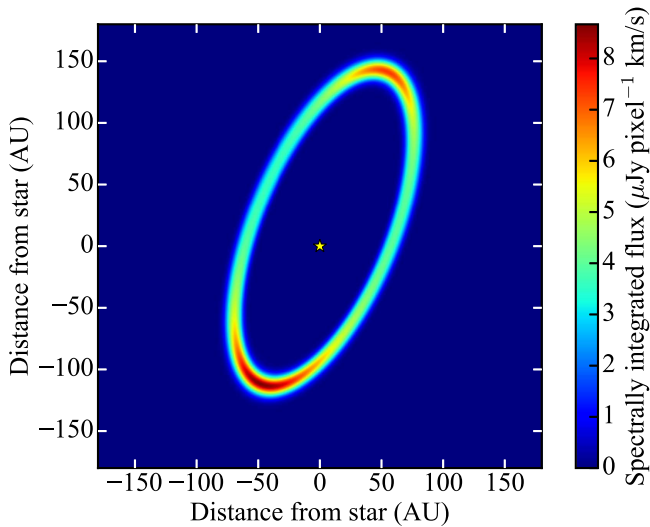
Figure 8. Model image for the maximum CO $J = 2$-1 flux enhancement expected at pericenter with respect to apocenter through steady-state CO production in the Fomalhaut ring. The model predicts a flux density enhancement of ∼14.5% at the pericenter ($\omega = 22°.5$) with respect to the apocenter location. However, this is for an infinitesimally short CO lifetime, much shorter than an orbital timescale; for the finite expected CO lifetime of 120 years, the peak is shifted by ∼19° in the direction of motion, which we here assumed to be clockwise. This shifts the peak to a true anomaly of $f \sim 3°.5$, or very close to the SE ansa. This model example assumes the best-fit orbital elements and ring width from the dust continuum fit, β Pictoris-like electron densities, a gas temperature equal to the blackbody temperature of ∼50K at the ring's distance to the star, a planetesimal strength $Q_D^\star = 10$, and a radially constant vertical aspect ratio of 0.06.

nonnegligible vertical thickness should present two enhancements at the location of the two ansae (see Marino et al. 2016 for the dependence of the azimuthal intensity distribution on a ring's scale height). To fully take this effect into account and demonstrate its impact on the measured pericenter or apocenter glow, we produce a simple model of CO in the Fomalhaut ring and produce a sky-projected model image using the RADMC-3D[15] radiative transfer code. In doing this, we first construct an eccentric CO ring model with radial mass distribution, inclination to the line of sight, position angle, forced eccentricity, and argument of pericenter equal to those of the dust ring. Then, we introduce the dependence of the CO surface density on the true anomaly as described above and derived in Appendix A. We assume the maximum possible pericenter versus apocenter CO mass enhancement for the best-fit $e_p \sim 0.06$ from the continuum observations, corresponding to ∼12% (for a $Q_D^\star$ of $10 \, \mathrm{J \, kg^{-1}}$). Furthermore, we make the simple assumptions that the gas kinetic temperature is equal to the blackbody temperature of the planetesimals and that the electron density follows the same radial dependence as found in β Pictoris.

In our model (see the spectrally integrated image in Figure 8), we assume a radially constant CO vertical aspect ratio equal to the average proper eccentricity of the planetesimals ($h \sim 0.06$), but we also consider extreme cases of a very small aspect ratio ($h \sim 0.0001$) and a larger one ($h \sim 0.14$, corresponding to the 3σ upper limit found for the HD 181327 ring; Marino et al. 2016). We find that in the infinitesimally vertically thin limit we recover the pericenter enhancement with respect to apocenter expected from our CO steady-state model from both

mass (12%) and excitation (∼2.5%) effects. In the vertically thick cases, the value of this ratio is slightly reduced due to the additional "background" effect of the ansae enhancement. Their absolute flux difference, however, remains unchanged, due to the projection effect being axisymmetric with respect to the ring's geometric center.

To conclude, the upper-limit pericenter versus apocenter enhancement predicted by our model (14.5%) is marginally consistent with our measurement from the current data set ($88 \pm 25\%$; see Section 3.5) at the 2.9σ level. If confirmed at high significance, this discrepancy would indicate the inability of our steady-state model to explain this asymmetry. In turn, this may favor a stochastic event such as the destruction of a large icy body near the belt's pericenter (as discussed in Section 4.2). Similarly, a recent impact was previously invoked to explain the observed CO asymmetry in the β Pictoris system (Dent et al. 2014), though this was recently ruled out through higher-resolution observations (Matrà et al. 2017).

Either way, a conclusive detection of this enhancement would allow us to determine the direction of orbital motion of the belt, and in turn whether its east or west side is nearest to Earth. This is because the finite lifetime of CO (∼120 years in such an optically thin environment) would cause either a tail in the direction of motion (in case of a stochastic event; see, e.g., Dent et al. 2014) or a ∼19° offset of the peak location (with respect to pericenter/apocenter, also in the direction of motion) due to CO pericenter/apocenter glow. Therefore, future, deeper ALMA observations of pericenter and apocenter are warranted to confirm this tentative evidence for asymmetry.

5. Conclusions

This work presented observations of CO $J = 2$-1 230 GHz emission in the Fomalhaut ring. Through spectrospatial filtering of the ALMA data cube, we detected line emission with an integrated line flux of $68 \pm 16 \, \mathrm{mJy \, km \, s^{-1}}$ at a radial velocity consistent with that of the star. We report the following findings:

1. The spectrospatial filtering method shows that the ring's sky-projected rotation axis matches that of the star (Le Bouquin et al. 2009), with the material at the SE ansa moving toward us. This however remains insufficient to determine the sense of rotation and in turn whether the NE side of the ring (observed to be brighter in *HST* scattered light imaging; Kalas et al. 2005) is in front of or behind the sky plane.

2. The radial location of the emission is consistent with that of the millimeter dust ring (as presented in MacGregor et al. 2017), indicating that both the observed CO and dust originate from the cometary belt at a distance of ∼136 au from the star.

3. CO $J = 2$-1 emission is optically thin and originates from a total CO gas mass of $(0.65$–$42) \times 10^{-7} \, M_\oplus$. This is consistent with the previous ALMA nondetection of the $J = 3$-2 transition (Matrà et al. 2015) and is in line with the CO excitation conditions observed in the β Pictoris disk.

4. At an age of 440 Myr, Fomalhaut hosts the oldest debris belt where gas emission colocated with dust emission has been detected to date. The amount of CO and the potential high amounts of H_2 (more typical of primordial protoplanetary disks) are insufficient to shield CO and

---

[15] http://www.ita.uni-heidelberg.de/dullemond/software/radmc-3d

allow it to survive over the system's lifetime. This implies that the observed CO is of secondary origin and originates from exocometary ices within the belt.

5. We evaluate the possibility of CO being produced from either stochastic destruction of a large icy body or steady-state release through the collisional cascade. We deem a stochastic collision possible but reasonably likely only for high total belt masses. On the other hand, in the steady-state scenario (as first described in Matrà et al. 2015), we combine the mass loss rate from the collisional cascade (producing CO) with the known CO photodissociation rate (destroying CO) to infer a $CO+CO_2$ exocometary mass fraction of 4.6%–76%. This is consistent with the other two debris belts where gas has been confirmed to be of exocometary origin, β Pictoris (Matrà et al. 2017) and HD 181327 (Marino et al. 2016).

6. As well as being similar to one another, exocometary CO $+CO_2$ mass fractions are consistent with observations of solar system comets, where this may be explained by similar blackbody temperatures and may indicate similar formation conditions in the original protoplanetary disk. We present a simple ISM inheritance model, showing that the $CO+CO_2$ mass fractions in exo- and solar system comets are consistent with all of the $CO+CO_2$ having been directly inherited from the ISM's $CO+CO_2$ ice and CO gas content. Increasingly accurate cometary abundance measurements are needed to distinguish between comet formation scenarios and to estimate the amount of $CO+CO_2$ that was lost through grain surface chemistry forming more complex organics or through gas release during the main-sequence phase of evolution, as observed here.

7. We report tentative evidence that most of the detected CO emission (49 ± 27)% originates near the ring's pericenter location derived by ALMA and *HST* high-resolution dust imaging. This may be due to a recent impact event that took place near pericenter, or to CO pericenter glow caused by the combined effect of (A) a steady-state mass loss rate enhancement at pericenter for an eccentric ring (for sufficiently high values of proper eccentricities e_p or sufficiently low planetesimal strengths $Q_D^\star$) and (B) molecular excitation effects due to the pericenter being closer to the central star.

8. We presented a model of CO pericenter or apocenter glow expected for exocometary CO released in eccentric belts. For a well-characterized dust belt such as Fomalhaut, the expected CO mass ratio at apocenter with respect to pericenter is only a function of the planetesimal strength $Q_D^\star$ and the mean proper eccentricity e_p. The model presented is general and indicates that we should expect asymmetric exocometary emission in eccentric gas-bearing debris disks, a prediction that may be tested by future ALMA observations. The highest possible CO flux enhancement at pericenter versus apocenter predicted in the Fomalhaut belt ($\sim$14.5%) is at the limit of being marginally consistent with our observations; if confirmed, a pericenter enhancement much higher than this prediction would rule out a steady-state scenario, proving instead that the observed CO must have originated from a recent impact between very large comets.

Appendix A
Dependence of Mass Loss Rate on the True Anomaly in a Steady-state Collisional Cascade

Here, we aim to derive the dependence of the solid mass loss rate $\dot{M}(D, f) = M(D, f)R_{col}(D, f)$ on the true anomaly f in an element of length along the ring ds and in a size bin between D and $D + dD$. Following Wyatt & Dent (2002), and explicitly marking the dependence of parameters on the true anomaly f, the collision rate of planetesimals of sizes in the range D_{im} to $D_{im} + dD_{im}$ on a planetesimal of size D is

$$R_{col}(D, D_{im}, f) = F(D, D_{im})\sigma(f)v_{rel}(f), \qquad (6)$$

where $\sigma(f)$ is the cross-sectional area per unit volume of planetesimals of all sizes, $v_{rel}(f)$ is the relative velocity of the impactor and the target, and $F(D, D_{im})$ is the collisional cross section of impactors of size D_{im} on the target of size D. Neglecting gravitational focusing, which in Fomalhaut becomes important only for bodies that are too large to participate in the collisional cascade (Wyatt & Dent 2002), the latter is expressed as

$$F(D, D_{im}) = \bar{\sigma}(D_{im})\left(1 + \frac{D}{D_{im}}\right)^2, \qquad (7)$$

where $\bar{\sigma}(D_{im}) = \sigma(D_{im})\left/ \int_{D_{min}}^{D_{max}} \sigma(D)dD\right.$ is the normalized cross section of the impactor, with D_{min} and D_{max} being the minimum and maximum size of solids participating in the collisional cascade.

The catastrophic collision rate for a planetesimal of size D from impactors of all sizes is then

$$R_{col}(D, f) = \sigma(f) v_{rel}(f) \int_{\max\{D_{cc}(f,D),D_{min}\}}^{D_{max}}$$
$$\times F(D, D_{im}) dD_{im}, \qquad (8)$$

where $D_{cc}(f, D)$ is the minimum impactor size for a collision to be catastrophic:

$$D_{cc}(f, D) = D(2Q_D^\star / v_{rel}^2(f))^{1/3}, \qquad (9)$$

where $Q_D^\star$ is the specific incident energy required for a catastrophic collision, that is, one where the largest collisional fragment has half the mass of the original target planetesimal.

We here assume that the relative velocity of planetesimals can be expressed as $v_{rel}(f) = v_{Kep}(f)\sqrt{1.25 e_p^2 + I^2}$ (e.g., Lissauer & Stewart 1993), and that the mean planetesimal inclinations $I \approx e_p$, where e_p is the mean proper eccentricity of planetesimals in the belt. This differs from the forced eccentricity e_{frc} in that the forced component can be seen as that imposed on all particle orbits through secular interaction with an unseen perturber, whereas the proper component can be interpreted as the "intrinsic" eccentricity of the particle and defines the width of the torus formed by particles orbiting the star with the same semimajor axis (see, e.g., Figure 2 in Wyatt et al. 1999). Therefore, while the mean proper eccentricity e_p determines the extent of orbit crossing and changes the relative velocity of collisions equally at any true anomaly, it is the forced eccentricity e_{frc} that introduces a dependence on the true anomaly on the Keplerian velocity, and hence on the relative velocity of collisions (see Equation (13)).

Following Pan et al. (2016), the linear number density, and hence the cross-sectional area density $\sigma(f)$ and the mass $M(D, f)$ in an element of length ds, depend on the inverse of the Keplerian velocity $\sigma(f) \propto 1/v_{Kep}(f)$. This means that the product $\sigma(f) v_{rel}(f)$ in Equation (8) is independent of the Keplerian velocity v_{Kep} and hence of the true anomaly f. However, the collision rate $R_{col}(D)$ remains dependent on f through the minimum size $D_{cc}(f, D)$ of impactors causing a catastrophic collision, which depends on the relative collision velocities $v_{rel}(f)$.

As shown in Wyatt et al. (1999), assuming that the steady-state size distribution follows the expression $n(D) \propto D^{2-3q}$ from D_{min} to D_{max} (Dohnanyi 1969), the integral in Equation (8) can be solved to obtain

$$\int_{\max\{D_{cc}(f,D),D_{min}\}}^{D_{max}} F(D, D_{im}) dD_{im} = \left(\frac{X(f)D}{D_{min}}\right)^{5-3q}$$
$$\times \left[1 + \frac{6q - 10}{(3q - 4)X(f)} + \frac{3q - 5}{(3q - 3)X(f)^2}\right], \qquad (10)$$

where $X(f) = D_{cc}(f, D)/D = (2Q_D^\star / v_{rel}^2(e_p, f))^{1/3}$ for $D_{cc}(f, D) > D_{min}$ and $X(f) = D_{min}/D$ for $D_{cc}(f, D) < D_{min}$. One can immediately notice that for sizes where all impactors above the minimum size always cause a catastrophic collision $(D_{cc}(f, D) < D_{min})$, the integral becomes simply the expression in the square brackets above, and its dependence on the true anomaly is lost. This has implications for the smallest particles in the size distribution, which we will come back to later. For (larger) sizes where $D_{cc}(f, D) > D_{min}$, assuming that the smallest and largest sizes D_{min} and D_{max} as well as the

slope of the collisional cascade parameterized by q are independent of the true anomaly, the azimuthal dependence of the collision rate can be expressed through v_{rel} as

$$R_{col}(D, f) \propto v_{rel}(f)^{2q - \frac{10}{3}}\left[1 + \frac{6q - 10}{(2Q_D^\star)^{\frac{1}{3}}(3q - 4)}\right.$$
$$\left. \times v_{rel}(f)^{\frac{2}{3}} + \frac{3q - 5}{(2Q_D^\star)^{\frac{2}{3}}(3q - 3)} v_{rel}(f)^{\frac{4}{3}}\right]. \qquad (11)$$

Since the dependence on the true anomaly enters the expression through the Keplerian velocity v_{Kep}, we can rewrite the above expression in terms of $v_{Kep}(f)$. Then, we assume a Dohnanyi (1969) size distribution ($q = 11/6$) and include the v_{Kep}^{-1} dependence of the mass $M(D, f)$ in the belt to obtain the dependence of the mass loss rate on v_{Kep}:

$$\dot{M}(D, f) \propto (\sqrt{2.25}\, e_p)^{\frac{1}{3}} v_{Kep}(f)^{-\frac{2}{3}}$$
$$\times \left[1 + \frac{2}{3}(2Q_D^\star)^{-\frac{1}{3}}(\sqrt{2.25}\, e_p v_{Kep}(f))^{\frac{2}{3}}\right.$$
$$\left. + \frac{1}{5}(2Q_D^\star)^{-\frac{2}{3}}(\sqrt{2.25}\, e_p v_{Kep}(f))^{\frac{4}{3}}\right], \qquad (12)$$

where the Keplerian velocity in the eccentric planetesimal belt can be expressed as (following Pan et al. 2016)

$$v_{Kep}(f) = \sqrt{\frac{GM_\star}{a}\frac{1 + 2e_{frc}\cos f + e_{frc}^2}{1 - e_{frc}^2}}, \qquad (13)$$

where G is the gravitational constant, $M_\star$ is the stellar mass, and a is the semimajor axis of the belt.

Equations (12) and (13) have implications for the predicted enhancement of pericenter with respect to apocenter (or vice versa), which we express as $1 - \dot{M}(f = 180°)/\dot{M}(f = 0°)$ and show in Figure 7. In particular, it can be shown that

$$e_p \rightarrow 0 \Rightarrow \frac{\dot{M}(f = 0°)}{\dot{M}(f = 180°)} \rightarrow \left(\frac{v_{Kep}(f = 0°)}{v_{Kep}(f = 180°)}\right)^{-\frac{2}{3}}$$
$$= \left(\frac{1 + e_{frc}}{1 - e_{frc}}\right)^{-\frac{2}{3}} < 1 \qquad (14)$$

and

$$e_p \rightarrow \infty \Rightarrow \frac{\dot{M}(f = 0°)}{\dot{M}(f = 180°)} \rightarrow \left(\frac{v_{Kep}(f = 0°)}{v_{Kep}(f = 180°)}\right)^{+\frac{2}{3}}$$
$$= \left(\frac{1 + e_{frc}}{1 - e_{frc}}\right)^{+\frac{2}{3}} > 1, \qquad (15)$$

meaning that a pericenter mass loss rate enhancement is expected for high proper eccentricities (since the high relative collision velocities at pericenter dominate over the mass enhancement at apocenter), whereas an apocenter mass loss rate enhancement is expected for low proper eccentricities (since the mass enhancement at apocenter dominates over the increase in collision velocities at pericenter). We note that in the limit of small proper eccentricities ($e_p \rightarrow 0$), the minimum impactor size $D_{cc}(f, D)$ to cause a catastrophic collision on a target D is much larger than the target itself ($D_{cc}(f, D) \gg D$).

This would create a collisional cascade where only the smallest of two colliding bodies is destroyed, while neither is destroyed if their sizes are similar.

It is also interesting to note that for small particles that can be destroyed by impactors of all sizes down to the minimum size (i.e., for particles where $D_{cc}(f, D) < D_{min}$) the collision rate R_{col} is independent of the true anomaly. This means that for sufficiently small particles the dependence of the mass loss rate on the true anomaly is driven purely by the azimuthal distribution of mass, leading to $\dot{M} \propto v_{Kep}(f)^{-1}$ and causing an apocenter enhancement even stronger than described by Equation (14) in the $e_p \rightarrow 0$ limit.

Appendix B
On the Mass Loss Rate of the Smallest Bodies in the Collisional Cascade

The mass loss rate $\dot{M}_{D_{min}}$ at which the smallest grains in the collisional cascade are removed from the system can be estimated through the collisional mass loss rate of grains just above the minimum size D_{min} in the cascade. As we will show in this section, the latter is well constrained observationally and can be calculated through their observed cross section $\sigma_{D_{min}}$, leading to their mass $M_{D_{min}}$, multiplied by their collision rate $R_{col}(D_{min})$.

For a thin ring such as Fomalhaut, the total mass of the smallest grains (in $M_\oplus$) can be expressed as a function of their total cross-sectional area $\sigma_{D_{min}} \sim \sigma_{tot}$ (in au^2, where we are assuming that these grains dominate the total observed cross-sectional area of the ring σ_{tot}) through

$$M_{D_{min}} = 2.5 \times 10^{-9} \rho \sigma_{tot} D_{min}, \qquad (16)$$

assuming grains of mass density ρ in $kg\ m^{-3}$, with D_{min} in μm. The total cross-sectional area can be expressed observationally as $\sigma_{tot} = 4\pi R^2 f$, where for Fomalhaut we take R to be the semimajor axis of the ring in au, and $f = L_{IR}/L_\star$ is the fractional luminosity of the ring. Then, we can assume D_{min} to be the blow-out size for blackbody grains around a star of a given luminosity and mass (in units of $L_\odot$ and $M_\odot$), leading to (e.g., Wyatt 2008)

$$M_{D_{min}} = 6.7 \times 10^{-5} R^2 f L_\star M_\star^{-1}. \qquad (17)$$

Around Fomalhaut, given a stellar mass of $1.92\ M_\odot$ (Mamajek 2012), a best-fit belt semimajor axis of 143.0 au (from ALMA continuum observations, MacGregor et al. 2017), and a stellar luminosity of $16.6\ L_\odot$ and fractional luminosity of 7.8×10^{-5} (from SED fitting, Kennedy & Wyatt 2014), we obtain a mass in small grains of $9.2 \times 10^{-4}\ M_\oplus$, which is within a factor of 2 of other values quoted by Zuckerman & Song (2012) and Acke et al. (2012).

The collision rate of grains of size D_{min} can also be calculated using Equations (8) and (10). These can be greatly simplified when considering particles impacting the smallest grains of the cascade, under the condition that $D_{cc}(f, D_{min}) < D_{min}$, or, in other words, collisions impacting the smallest grains (dominated by grains of the same size, since these dominate the belt's cross-sectional area) are always catastrophic. Given the definition of $D_{cc}(f, D)$ (Equation (9)), this is the case for $D_{cc}(f, D_{min})/D_{min} = (2Q_{D_{min}}^\star / v_{rel}^2(e_p))^{1/3} < 1$, or $Q_{D_{min}}^\star < v_{rel}^2(e_p)/2$. In the Fomalhaut ring, given a best-fit mean proper eccentricity of 0.06

(MacGregor et al. 2017), $v_{rel} \sim 0.31\ km\ s^{-1}$, leading to a condition $Q_{D_{min}}^\star \lesssim 5 \times 10^4\ J\ kg^{-1}$ for the smallest grains in the cascade. Using the compilation of $Q_D^\star$ versus size values in Krijt & Kama (2014), we find that this is always the case for grains larger than the blow-out size (7.2 μm for compact SiO_2 blackbody grains and 18.7 μm for pure water ice grains). This remains valid if the smallest grains in the cascade are larger than the blow-out limit (as argued in Krijt & Kama 2014).

Then, $X(f) = D_{min}/D$ with $D = D_{min}$ implies $X(f) = 1$ in Equation (10). Estimating the cross section per unit volume of grains (in au^{-1}) of all sizes as $\sigma = \sigma_{tot}/V$ where V is the volume of the ring in au^3, this reduces the expression for the collision rate of the smallest grains (Equation (8), here in yr^{-1}) to

$$R_{col}(D_{min}) = 0.21 \frac{\sigma_{tot} v_{rel}}{V} \left[1 + \frac{6q - 10}{(3q - 4)} + \frac{3q - 5}{(3q - 3)} \right]$$
$$\times\ for\ Q_{D_{min}}^\star < v_{rel}^2(e_p)/2, \qquad (18)$$

where v_{rel} is in $km\ s^{-1}$. We immediately note that the collision rate of these grains is now independent of $Q_{D_{min}}^\star$, removing the considerable amount of uncertainty introduced if calculating this collision rate for the largest bodies in the cascade, as previously worked out in Matrà et al. (2015) from the results of Wyatt & Dent (2002), as well as other works (Kennedy et al. 2015; Marino et al. 2016; Kral et al. 2017; Matrà et al. 2017). Expressing the cross-sectional area as a function of the belt's fractional luminosity, inserting the definition of v_{rel} with the assumption $e_p = I$, and taking the volume of the belt to be that of a narrow ring with constant aspect ratio ($V = 4\pi R^2 \Delta R I$, where ΔR is the width of the belt in au), we obtain the general expression

$$R_{col}(D_{min}) = 0.32 \frac{v_{Kep} f}{\Delta R} \left[1 + \frac{6q - 10}{(3q - 4)} + \frac{3q - 5}{(3q - 3)} \right]$$
$$= 9.6 \frac{M_\star^{0.5} f}{R^{0.5} \Delta R} \left[1 + \frac{6q - 10}{(3q - 4)} + \frac{3q - 5}{(3q - 3)} \right], \qquad (19)$$

which for $q = 11/6$, as is the case for the Fomalhaut belt, becomes

$$R_{col}(D_{min}) = 17.9\ M_\star^{0.5} f R^{-0.5} \Delta R^{-1}. \qquad (20)$$

This formula differs from Equation (25) in Wyatt et al. (2007) and Equation (B4) in Zuckerman & Song (2012) by a factor of ~ 1.4. The difference lies in two simplifying assumptions taken by those authors: (1) the relative collision velocities are set only by the vertical motion of particles in the disk, so that $v_{rel}/v_{Kep} \sim \sin(I) \sim I$ rather than $v_{rel}/v_{Kep} = \sqrt{1.25 e_p^2 + I^2} \sim \sqrt{2.25} I$, as assumed here; (2) particles of size D_{min} collide only with particles of the same size D_{min}, so that the integral in Equation (10), corresponding to the expression in square brackets in Equation (18), is independent of the slope of the size distribution and equal to 4, rather than 28/15 (for $q = 11/6$). In the Fomalhaut belt, we find that the smallest bodies will collide at a rate of $1.2 \times 10^{-5}\ yr^{-1}$, corresponding to a collision timescale of 8.5×10^4 years. This is similar to the timescale derived by Zuckerman & Song (2012),

but almost two orders of magnitude longer than the timescale derived by Acke et al. (2012). We divert the reader to Appendix C in Zuckerman & Song (2012) for a detailed discussion of this discrepancy.

Finally, combining the mass of small grains $M_{D_{\min}}$ with their collision rate $R_{\rm col}(D_{\min})$ above, we obtain a simple expression for the mass loss rate $\dot{M}_{D_{\min}}$ (in $M_\oplus$ Myr^{-1}) of grains at the bottom of the cascade:

$$\dot{M}_{D_{\min}} = 1.2 \times 10^3 \, R^{1.5} \Delta R^{-1} f^2 L_\star M_\star^{-0.5}, \qquad (21)$$

which is well constrained observationally through SED fitting (yielding stellar properties and the fractional luminosity) and resolved imaging of the belt (yielding accurate values of the belt radius and width). This allows us to derive a mass loss rate of the smallest grains in the Fomalhaut belt of $1.1 \times 10^{-2} \, M_\oplus$ Myr^{-1}, or 2.1×10^{12} g s^{-1}. The latter value is very close to the mass loss rate obtained from the modeling results of Wyatt & Dent (2002) for grains $\sim 10\,\mu m$ in size ($\sim 0.01 \, M_\oplus$ Myr^{-1}), although it differs substantially from the value of $\sim 0.1 \, M_\oplus$ Myr^{-1} obtained by Matrà et al. (2015) derived for the largest bodies participating in the cascade. This unexpected difference in mass loss rate is likely due to the fact that the Wyatt & Dent (2002) model assumes a $q = 11/6$ size distribution, typical of a collisional cascade where the planetesimal strength $Q_D^\star$ is independent of size, but then uses a $Q_D^\star$ varying with size to calculate collision rates, leading to an inconsistency that causes the unexpected result of a mass loss rate that varies with particle size.

References

Acke, B., Min, M., Dominik, C., et al. 2012, A&A, 540, A125
Aumann, H. H. 1985, PASP, 97, 885
Benz, W., & Asphaug, E. 1999, Icar, 142, 5
Beust, H., Augereau, J.-C., Bonsor, A., et al. 2014, A&A, 561, A43
Biver, N., Bockelée-Morvan, D., Colom, P., et al. 2002, EM&P, 90, 5
Boley, A. C., Payne, M. J., Corder, S., et al. 2012, ApJL, 750, L21
Bottke, W. F., Durda, D. D., Nesvorný, D., et al. 2005, Icar, 175, 111
Brandeker, A. 2011, ApJ, 729, 122
Brandeker, A., Cataldi, G., Olofsson, G., et al. 2016, A&A, 591, A27
Cataldi, G., Brandeker, A., Olofsson, G., et al. 2015, A&A, 574, L1
Chiang, E., Kite, E., Kalas, P., Graham, J. R., & Clampin, M. 2009, ApJ, 693, 734
Collings, M. P., Anderson, M. A., Chen, R., et al. 2004, MNRAS, 354, 1133
Currie, T., Debes, J., Rodigas, T. J., et al. 2012, ApJL, 760, L32
Czechowski, A., & Mann, I. 2007, ApJ, 660, 1541
Dent, W. R. F., Wyatt, M. C., Roberge, A., et al. 2014, Sci, 343, 1490
Dohnanyi, J. S. 1969, JGR, 74, 2531
Favre, C., Cleeves, L. I., Bergin, E. A., Qi, C., & Blake, G. A. 2013, ApJL, 776, L38
Fernández, R., Brandeker, A., & Wu, Y. 2006, ApJ, 643, 509
Fomalont, E., van Kempen, T., Kneissl, R., et al. 2014, Msngr, 155, 19
Fraser, W. C., Brown, M. E., Morbidelli, A., Parker, A., & Batygin, K. 2014, ApJ, 782, 100
Galicher, R., Marois, C., Zuckerman, B., & Macintosh, B. 2013, ApJ, 769, 42
Gontcharov, G. A. 2006, AstL, 32, 759
Gray, R. O., & Garrison, R. F. 1989, ApJS, 70, 623
Grigorieva, A., Thébault, P., Artymowicz, P., & Brandeker, A. 2007, A&A, 475, 755
Hales, A. S., Barlow, M. J., Crawford, I. A., & Casassus, S. 2017, MNRAS, 466, 3582
Holland, W. S., Greaves, J. S., Dent, W. R. F., et al. 2003, ApJ, 582, 1141
Holland, W. S., Greaves, J. S., Zuckerman, B., et al. 1998, Natur, 392, 788
Janson, M., Carson, J. C., Lafrenière, D., et al. 2012, ApJ, 747, 116
Janson, M., Quanz, S. P., Carson, J. C., et al. 2015, A&A, 574, A120
Johansen, A., Mac Low, M.-M., Lacerda, P., & Bizzarro, M. 2015, SciA, 1, 1500109

Kalas, P., Graham, J. R., Chiang, E., et al. 2008, Sci, 322, 1345
Kalas, P., Graham, J. R., & Clampin, M. 2005, Natur, 435, 1067
Kalas, P., Graham, J. R., Fitzgerald, M. P., & Clampin, M. 2013, ApJ, 775, 56
Kennedy, G. M., Matrà, L., Marmier, M., et al. 2015, MNRAS, 449, 3121
Kennedy, G. M., & Wyatt, M. C. 2011, MNRAS, 412, 2137
Kennedy, G. M., & Wyatt, M. C. 2014, MNRAS, 444, 3164
Kenyon, S. J., & Bromley, B. C. 2008, ApJS, 179, 451
Kenyon, S. J., & Bromley, B. C. 2015, ApJ, 811, 60
Kenyon, S. J., Currie, T., & Bromley, B. C. 2014, ApJ, 786, 70
Kral, Q., Matra, L., Wyatt, M., & Kennedy, G. 2017, arXiv:1703.10693
Kral, Q., Wyatt, M., Carswell, R. F., et al. 2016, MNRAS, 461, 845
Krijt, S., & Kama, M. 2014, A&A, 566, L2
Lawler, S. M., Greenstreet, S., & Gladman, B. 2015, ApJL, 802, L20
Le Bouquin, J.-B., Absil, O., Benisty, M., et al. 2009, A&A, 498, L41
Le Roy, L., Altwegg, K., Balsiger, H., et al. 2015, A&A, 583, A1
Lissauer, J. J., & Stewart, G. R. 1993, in Protostars and Planets III, ed. E. H. Levy & J. I. Lunine (Tucson, AZ: Univ. Arizona Press), 1061
Luspay-Kuti, A., Mousis, O., Ha ssig, M., et al. 2016, SciA, 2, e1501781
MacGregor, M. A., et al. 2017, arXiv:1705.05867
Mamajek, E. E. 2012, ApJ, 754, L20
Mamajek, E. E., & Bell, C. P. M. 2014, MNRAS, 445, 2169
Marboeuf, U., & Schmitt, B. 2014, Icar, 242, 225
Marboeuf, U., Schmitt, B., Petit, J.-M., Mousis, O., & Fray, N. 2012, A&A, 542, A82
Marengo, M., Stapelfeldt, K., Werner, M. W., et al. 2009, ApJ, 700, 1647
Marino, S., Matrà, L., Stark, C., et al. 2016, MNRAS, 460, 2933
Marino, S., Wyatt, M. C., Panić, O., et al. 2017, MNRAS, 465, 2595
Marsh, K. A., Velusamy, T., Dowell, C. D., Grogan, K., & Beichman, C. A. 2005, ApJL, 620, L47
Matrà, L., Dent, W. R. F., Wyatt, M. C., et al. 2017, MNRAS, 464, 1415
Matrà, L., Panić, O., Wyatt, M. C., & Dent, W. R. F. 2015, MNRAS, 447, 3936
McMullin, J. P., Waters, B., Schiebel, D., Young, W., & Golap, K. 2007, in ASP Conf. Ser. 376, Astronomical Data Analysis Software and Systems XVI, ed. R. A. Shaw, F. Hill, & D. J. Bell (San Francisco, CA: ASP), 127
Min, M., Kama, M., Dominik, C., & Waters, L. B. F. M. 2010, A&A, 509, L6
Morbidelli, A., Lunine, J. I., O'Brien, D. P., Raymond, S. N., & Walsh, K. J. 2012, AREPS, 40, 251
Mumma, M. J., & Charnley, S. B. 2011, ARA&A, 49, 471
Neuhäuser, R., Hohle, M. M., Ginski, C., et al. 2015, MNRAS, 448, 376
Nilsson, R., Brandeker, A., Olofsson, G., et al. 2012, A&A, 544, A134
Öberg, K. I., van Dishoeck, E. F., & Linnartz, H. 2009, A&A, 496, 281
Pan, M., Nesvold, E. R., & Kuchner, M. J. 2016, ApJ, 832, 81
Pätzold, M., Andert, T., Hahn, M., et al. 2016, Natur, 530, 63
Pearce, T. D., Wyatt, M. C., & Kennedy, G. M. 2015, MNRAS, 448, 3679
Pontoppidan, K. M., Salyk, C., Bergin, E. A., et al. 2014, in Protostars and Planets VI, ed. H. Beuther, R. S. Klessen, C. P. Dullemond, & T. Henning (Tucson, AZ: Univ. Arizona Press), 363
Quillen, A. C. 2006, MNRAS, 372, L14
Redfield, S. 2007, ApJL, 656, L97
Ricci, L., Testi, L., Maddison, S. T., & Wilner, D. J. 2012, A&A, 539, L6
Roberge, A., Feldman, P. D., Weinberger, A. J., Deleuil, M., & Bouret, J.-C. 2006, Natur, 441, 724
Rotundi, A., Sierks, H., Della Corte, V., et al. 2015, Sci, 347, aaa3905
Schlichting, H. E., Fuentes, C. I., & Trilling, D. E. 2013, AJ, 146, 36
Shannon, A., Wu, Y., & Lithwick, Y. 2016, ApJ, 818, 175
Stapelfeldt, K. R., Holmes, E. K., Chen, C., et al. 2004, ApJS, 154, 458
Stern, S. A., & Colwell, J. E. 1997, ApJ, 490, 879
Tamayo, D. 2014, MNRAS, 438, 3577
van Dishoeck, E. F., Helmich, F. P., de Graauw, T., et al. 1996, A&A, 315, L349
van Leeuwen, F. 2007, A&A, 474, 653
Visser, R., van Dishoeck, E. F., & Black, J. H. 2009, A&A, 503, 323
Weissman, P. R. 2007, in IAU Symp. 236, Near Earth Objects, our Celestial Neighbors: Opportunity and Risk, ed. G. B. Valsecchi, D. Vokrouhlický, & A. Milani (Cambridge: Cambridge Univ. Press), 441
White, J. A., Boley, A. C., Dent, W. R. F., Ford, E. B., & Corder, S. 2017, MNRAS, 466, 4201
Wyatt, M. C. 2008, ARA&A, 46, 339
Wyatt, M. C., & Dent, W. R. F. 2002, MNRAS, 334, 589
Wyatt, M. C., Dermott, S. F., Telesco, C. M., et al. 1999, ApJ, 527, 918
Wyatt, M. C., Panić, O., Kennedy, G. M., & Matrà, L. 2015, Ap&SS, 357, 103
Wyatt, M. C., Smith, R., Greaves, J. S., et al. 2007, ApJ, 658, 569
Zuckerman, B., & Song, I. 2012, ApJ, 758, 77